Nodal topology in d-wave superconducting monolayer FeSe

Takeru Nakayama,[1,*] Tatsuya Shishidou,[2] and Daniel F. Agterberg[2]

[1]*The Institute for Solid State Physics, The University of Tokyo, 5-1-5 Kashiwanoha, Kashiwa, Chiba 277-8581, Japan*
[2]*Department of Physics, University of Wisconsin–Milwaukee, Milwaukee, Wisconsin 53211, USA*

A nodeless d-wave state is likely in superconducting monolayer FeSe on $SrTiO_3$. The lack of nodes is surprising but has been shown to be a natural consequence of the observed small interband spin-orbit coupling. Here we examine the evolution from a nodeless state to the nodal state as this spin-orbit coupling is increased from a topological perspective. We show that this evolution depends strongly on the orbital content of the superconducting degrees of freedom. In particular, there are two d-wave solutions, which we call orbitally trivial and orbitally nontrivial. In both cases, the nodes carry a ± 2 topological winding number that originates from a chiral symmetry. However, the momentum space distribution of the positive and negative charges is different for the two cases, resulting in a different evolution of these nodes as they annihilate to form a nodeless superconductor. We further show that the orbitally trivial and orbitally nontrivial nodal states exhibit different Andreev flat band spectra at the edge.

I. INTRODUCTION

Monolayer FeSe grown on $SrTiO_3$ has generated much attention due to its high superconducting transition temperature T_c, which is higher than all the other Fe-based superconductors [1]. Quasiparticle interference [2] experiments and scanning tunneling microscopy [1,3] suggest a plain s-wave pairing state. Angle-resolved photoemission spectroscopy (ARPES) [4–7] also supports this point of view by observing a fully gapped superconducting state, although with a nontrivial anisotropy [7]. The appearance of an s-wave pairing state in this material seems at odds with the understanding that superconductivity in Fe-based materials is due to repulsive electron-electron interactions and presents a puzzle. Furthermore, monolayer FeSe lacks the hole pockets about the Γ point of the Brillouin zone (BZ) which exist in other iron pnictide compounds. This suggests that the usual $s_\pm$-wave pairing [8,9] due to spin fluctuations about a collinear antiferromagnetic state with a wave vector that originates from the momentum difference between electron and hole pockets is less likely as a pairing mechanism. This has led to a debate about the nature of the pairing state in monolayer FeSe. Some proposals include (for a review see Ref. [10]) a conventional s-wave pairing state [2,11], an incipient s-wave pairing state [12], an extended s-wave pairing state [13], a fully gapped spin-triplet pairing state [14], and a nodeless d-wave pairing state [15,16].

Recently, we revisited the nature of the magnetic correlations and the pairing state in monolayer FeSe [16,17]. Inelastic neutron scattering in single-crystal FeSe [18] has found that, in addition to collinear antiferromagnetic fluctuations, there are also fluctuations associated with translation-invariant checkerboard antiferromagnetic (CB-AFM) order.

First-principles spin-spiral calculations [17] also report the enhanced CB-AFM fluctuations in monolayer FeSe, finding that this system sits at a quantum spin-fluctuation-mediated spin paramagnetic ground state. Motivated by the presence of CB-AFM fluctuations, a symmetry-based $k \cdot p$ theory assuming a single M-point electronic representation was used to describe fermions coupled to these fluctuations [16,19]. This theory predicts a fully gapped, nodeless d-wave state [16]. Although, typically, symmetry arguments imply that such a d-wave state should be nodal [20], this theory reveals that nodal points emerge only if the relevant interband spin-orbit coupling energy is larger than the superconducting gap. This theory thereby naturally accounts for the gap minima that are observed along the expected nodal momentum directions of the d-wave state [7].

A natural question is, What is the mechanism that leads to a nodeless, fully gapped d-wave superconducting state? Indeed, one can ask how such nodeless states are more generally achieved when symmetry arguments would dictate nodes. Here we address this question through an examination of the nodal d-wave state. This question falls naturally into the growing research on topological systems, which originally started with gapped systems [21] such as quantum Hall systems and topological insulators in which surface states are characterized by "bulk-edge correspondence." More recently, this was extended to gapless systems such as Weyl and Dirac semimetals [22] and unconventional superconductors [23]. In unconventional superconductors that are nodal, that is, that have momenta with zero gap, it is known that the sign change of the pairing potential on the Fermi surface leads to dispersionless Andreev bound states at a surface of the system. These states are characterized through topological arguments [24,25]. Therefore, studies of nodes in unconventional superconductors are important not only to reveal the pairing mechanism but also to clarify the topological surface states.

_____
*t.nakayama@issp.u-tokyo.ac.jp

Although d-wave superconducting states typically have topologically protected nodes in one-band systems, these nodal points can be annihilated in multiband superconductors [26,27]. Indeed, it has been pointed out that the merging nodal points near the Γ point have winding numbers of opposite sign in Fe-based superconductors [28]. In addition, a nodeless d-wave superconductor has also been discussed in the context of cuprates [29]. These works did not include spin-orbit coupling, which is essential in our theory. Our work highlights the annihilation of nodes solely due to spin-orbit coupling and demonstrates that the nodal charge is protected by a chiral symmetry that is the product of time-reversal and particle-hole symmetries. Furthermore, we find that the nodal annihilation depends upon the orbital structure of the d-wave gap. In particular, we find two types of d-wave pairing: (a) orbitally trivial usual d-wave anisotropy with a $k_x k_y$ momentum dependence and (b) orbitally nontrivial with no momentum dependence. For the latter case, nodal annihilation arises in a natural and straightforward manner, while for the orbitally trivial case, the annihilation is much less straightforward, proceeding initially through the creation of additional nodes which then annihilate with the original nodes as the interband spin-orbit coupling is decreased.

The remainder of this paper is organized as follows. In Sec. II, we introduce the symmetry-based effective model that describes the electronic excitations that stem from a single M-point representation of the BZ; these representations are fourfold degenerate and thus lead to two bands. We then briefly review the emergence of nodal points due to interband spin-orbit coupling. In Sec. III, we give the topological charges for these nodal points as a $2\mathbb{Z}$ invariant and show that there are topologically distinguished phases which manifest themselves through the presence of dispersionless Andreev surface states. The results are summarized in Sec. IV.

II. MODEL

In this section, we present a brief review of the low-energy symmetry-based $\boldsymbol{k} \cdot \boldsymbol{p}$-like theory that describes the electronic states of monolayer FeSe in the vicinity of the Fermi level [16]. Density functional theory calculations show that two states, which are $\boldsymbol{k}$-dependent linear combinations of Fe $\{xz, yz\}$ and $x^2 - y^2$ orbitals, which are the two electronic M-point representations M_1 and M_3 using the nomenclature of Ref. [19], are dominant at the Fermi level around the M point. These states can be described as originating from a single M-point fourfold electronic representation (with two orbital and two spin degrees of freedom) through an effective $\boldsymbol{k} \cdot \boldsymbol{p}$ theory. The simplicity of this model allows insight into the underlying physics that cannot be found using a theoretical model simply based on ten orbital and two spin degrees of freedom. In addition, it captures the relevant physics of the superconducting state that appears in theories of monolayer FeSe that include two M-point representations [14].

In this theory, the normal-state Hamiltonian is

$$H_0(\boldsymbol{k}) = \epsilon_0 \tau_0 \sigma_0 + \gamma_{xy} \tau_z \sigma_0 + \tau_x [\gamma_x \sigma_y + \gamma_y \sigma_x], \quad (1)$$

where $\boldsymbol{k} = (k_x, k_y)$ is the momentum measured from the M point of the BZ and the τ_i (σ_i) matrices describe the two orbital (spin) degrees of freedom. The τ_x term is
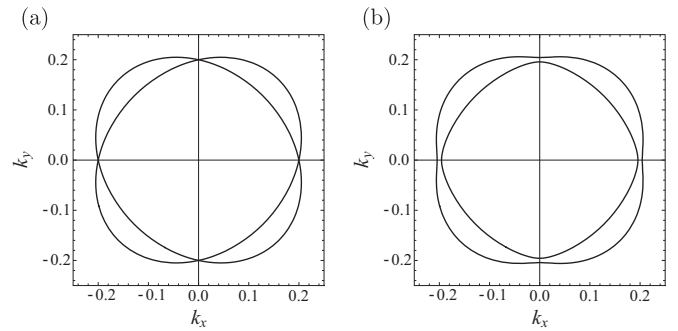

FIG. 1. Fermi surfaces in normal states (a) without spin-orbit coupling and (b) with spin-orbit coupling $v_{so} = 12$ meV Å. The units of horizontal and vertical axes are Å^{-1}. The other parameters are given in the text.

the interband spin-orbit coupling that plays an essential role in the d-wave superconducting state. This term has a magnitude that is related to the on-site spin-orbit coupling but is also determined by other factors and can be small even if the on-site spin-orbit coupling is substantial. The Fermi surface, as observed by ARPES, is reasonably described when we choose $\epsilon_0 = \epsilon_0(\boldsymbol{k}) = (k_x^2 + k_y^2)/2m - \mu$, $\gamma_{xy} = \gamma_{xy}(\boldsymbol{k}) = a k_x k_y$, $\gamma_x = \gamma_x(\boldsymbol{k}) = v_{so} k_x$, $\gamma_y = \gamma_y(\boldsymbol{k}) = v_{so} k_y$, and parameters $\mu = 55$ meV, $1/(2m) = 1375$ meV Å^2, $a = 600$ meV Å^2, and $|v_{so}| \leqslant 15$ meV Å. The normal-state dispersions are given by $\xi^{\pm} = \epsilon_0 \pm \sqrt{\gamma_x^2 + \gamma_y^2 + \gamma_{xy}^2}$, which have positive helicity and negative helicity, respectively. Figures 1(a) and 1(b) show the Fermi surfaces without spin-orbit coupling and with spin-orbit coupling $v_{so} = 12$ meV Å, respectively.

Superconducting pairing is assumed to be induced by the fluctuations associated with translation-invariant CB-AFM. This yields a d_{xy}-like pairing state. Importantly, for this paper, there are two such pairing states that are described in more detail below. The Hamiltonian is given by the following in the Bogoliubov–de Gennes form:

$$H(\boldsymbol{k}) = \Gamma_z (\epsilon_0 \tau_0 \sigma_0 + \gamma_{xy} \tau_z \sigma_0 + \gamma_x \tau_x \sigma_y)$$
$$+ \gamma_y \Gamma_0 \tau_x \sigma_x + i \Gamma_y (\Delta_{d,0} \tau_0 + \Delta_{d,z} \tau_z) i \sigma_y, \quad (2)$$

where the Γ_i matrices describe the particle-hole degree of freedom,

$$\Delta_{d,0} = \Delta_{d,0}(\boldsymbol{k}) = \Delta_2 k_x k_y / k_0^2,$$
$$\Delta_{d,z} = \Delta_{d,z}(\boldsymbol{k}) = \Delta_0, \quad (3)$$

and we take the typical Fermi wave vector $k_0 = 0.2$ Å^{-1}. The two gap functions $\Delta_{d,0}$ and $\Delta_{d,z}$ are the two d_{xy} pairing degrees of freedom mentioned above. The pairing term $\Delta_{d,0} \tau_0$ represents an orbitally trivial and usual d_{xy} pairing with a $k_x k_y$ momentum dependence. $\Delta_{d,z} \tau_z$ represents an orbitally nontrivial pairing state with no momentum dependence; it also has d_{xy} pairing symmetry due to the τ_z orbital dependence and the different symmetries of the two orbitals that give rise to this gap function. In general, since both $\Delta_{d,0}$ and $\Delta_{d,z}$ channels have the same symmetry, the gap function will be a linear combination of both these pairing channels.

In order to gain a deeper understanding of these two types of d_{xy} order, it is convenient to change basis from the orbital basis to the band basis. The Hamiltonian in (2) can be written in block diagonal form with two 4×4 matrices. One of these matrices is

$$
\begin{bmatrix}
\epsilon_0 + \gamma_{xy} & \gamma_y - i\gamma_x & 0 & \Delta_{d,0} + \Delta_{d,z} \\
\gamma_y + i\gamma_x & \epsilon_0 - \gamma_{xy} & -\Delta_{d,0} + \Delta_{d,z} & 0 \\
0 & -\Delta_{d,0} + \Delta_{d,z} & -\epsilon_0 + \gamma_{xy} & \gamma_y + i\gamma_x \\
\Delta_{d,0} + \Delta_{d,z} & 0 & \gamma_y - i\gamma_x & -\epsilon_0 - \gamma_{xy}
\end{bmatrix},
\tag{4}
$$

while the other matrix is given by transforming $\Delta_i \to -\Delta_i$ and $\gamma_x \to -\gamma_x$. Performing a unitary transformation that diagonalizes the normal part of the Hamiltonian we obtain in the band basis, we find

$$
\begin{bmatrix}
\epsilon_0 + \sqrt{\gamma_x^2 + \gamma_y^2 + \gamma_{xy}^2} & \Delta_{d,0} + \frac{\Delta_{d,z}\gamma_{xy}}{\sqrt{\gamma_x^2+\gamma_y^2+\gamma_{xy}^2}} & 0 & \frac{\Delta_{d,z}(\gamma_y - i\gamma_x)}{\sqrt{\gamma_x^2+\gamma_y^2+\gamma_{xy}^2}} \\
\Delta_{d,0} + \frac{\Delta_{d,z}\gamma_{xy}}{\sqrt{\gamma_x^2+\gamma_y^2+\gamma_{xy}^2}} & -\epsilon_0 - \sqrt{\gamma_x^2 + \gamma_y^2 + \gamma_{xy}^2} & \frac{\Delta_{d,z}(\gamma_y - i\gamma_x)}{\sqrt{\gamma_x^2+\gamma_y^2+\gamma_{xy}^2}} & 0 \\
0 & \frac{\Delta_{d,z}(\gamma_y + i\gamma_x)}{\sqrt{\gamma_x^2+\gamma_y^2+\gamma_{xy}^2}} & \epsilon_0 - \sqrt{\gamma_x^2 + \gamma_y^2 + \gamma_{xy}^2} & \Delta_{d,0} - \frac{\Delta_{d,z}\gamma_{xy}}{\sqrt{\gamma_x^2+\gamma_y^2+\gamma_{xy}^2}} \\
\frac{\Delta_{d,z}(\gamma_y + i\gamma_x)}{\sqrt{\gamma_x^2+\gamma_y^2+\gamma_{xy}^2}} & 0 & \Delta_{d,0} - \frac{\Delta_{d,z}\gamma_{xy}}{\sqrt{\gamma_x^2+\gamma_y^2+\gamma_{xy}^2}} & -\epsilon_0 + \sqrt{\gamma_x^2 + \gamma_y^2 + \gamma_{xy}^2}
\end{bmatrix}.
\tag{5}
$$

This band basis clarifies that the Hamiltonian has both intraband and interband pairings, as is the case in other proposals for nodeless d-wave superconductors [27]. The interband pairing arises only from the orbitally nontrivial $\Delta_{d,z}$ (in combination with the interband spin-orbit coupling). The intraband pairing contains both pairing channels. In this case, the orbitally nontrivial $\Delta_{d,z}$ channel explicitly gains d-wave momentum anisotropy through the γ_{xy} normal-state term. Figure 2 shows the pairing anisotropy in the case of only orbitally trivial pairing [Fig. 2(a)] and the orbitally nontrivial one in the band basis [Fig. 2(b)]. Note that here only spin-singlet pairing is considered. In general, there can be mixing of spin-singlet and -triplet pairings due to the interband spin-orbit coupling.

The interband pairing in the band basis is essential to generate a gapless superconducting d_{xy} state, provided the interband spin-orbit coupling is sufficiently small. To understand how a large interband spin-orbit coupling gives rise to nodal points, it is useful to consider the quasiparticle dispersion for Hamiltonian (2). This is given by

$$
E_\pm(\boldsymbol{k}) = \sqrt{\epsilon_0^2 + \gamma_{xy}^2 + \gamma_x^2 + \gamma_y^2 + \Delta_{d,0}^2 + \Delta_{d,z}^2 \pm 2\sqrt{(\epsilon_0\gamma_{xy} + \Delta_{d,0}\Delta_{d,z})^2 + (\gamma_x^2 + \gamma_y^2)(\epsilon_0^2 + \Delta_{d,z}^2)}}.
\tag{6}
$$

Notice that there are also two negative quasiparticle dispersions $-E_\pm(\boldsymbol{k})$ due to chiral symmetry. Along the nodal direction $k_y = 0$, so that $\gamma_{xy} = \gamma_y = \Delta_{d,0} = 0$, yielding $E_\pm(\boldsymbol{k}) = \left| \sqrt{\epsilon_0^2 + \Delta_{d,z}^2} \pm |\gamma_x| \right|$. Therefore, the following equation must be satisfied at the nodal points (labeled $\boldsymbol{k}^*$):

$$
\epsilon_0^2 = \gamma_x^2 - \Delta_{d,z}^2.
\tag{7}
$$

This means that once the interband spin-orbit coupling satisfies $|\gamma_x| > \Delta_{d,z}$, nodal points exist. As the interband spin-orbit coupling is reduced, there is consequently a transition from a nodal d_{xy} state to a fully gapped d_{xy} state, which is the focus of the remainder of this paper. Note that a generic consequence of this theory is that gap minima in the fully gapped state are along the nodal directions; this agrees with what is observed in ARPES measurements.

III. NODAL TOPOLOGICAL CHARGES AND ANDREEV FLAT-BAND STATES

A. Nodal topological charges

Now we examine how the fully gapped d_{xy} state appears as the interband spin-orbit coupling is reduced. In particular,

for sufficiently large interband spin-orbit coupling we have a nodal d_{xy} state, and we examine the topological charge of the nodal points. We show that topological charge at the nodal points can be defined as a $2\mathbb{Z}$ invariant. The key symmetries in defining this charge are time reversal (with operator T) and particle-hole conjugation (with operator C). These act on $H(\boldsymbol{k})$ as

$$
T H(\boldsymbol{k}) T^{-1} = H(-\boldsymbol{k}),
\tag{8}
$$

$$
C H(\boldsymbol{k}) C^{-1} = -H(-\boldsymbol{k}),
\tag{9}
$$

where $T = K\Gamma_0\tau_0(i\sigma_y)$, $C = K\Gamma_x\tau_0\sigma_0$, and K is the complex conjugate operator. Since $T^2 = -1$ and $C^2 = 1$, this Hamiltonian belongs to Altland-Zirnbauer class DIII [30]. Furthermore, we define a chiral operator S,

$$
S = -iTC = \Gamma_x\tau_0\sigma_y.
\tag{10}
$$

Since chiral symmetry is preserved and S anticommutes with $H(\boldsymbol{k})$, $H(\boldsymbol{k})$ can be written in block off-diagonal form using the basis in which S is diagonal:

$$
H(\boldsymbol{k}) \to V H(\boldsymbol{k}) V^\dagger = \begin{bmatrix} 0 & q(\boldsymbol{k}) \\ q^\dagger(\boldsymbol{k}) & 0 \end{bmatrix},
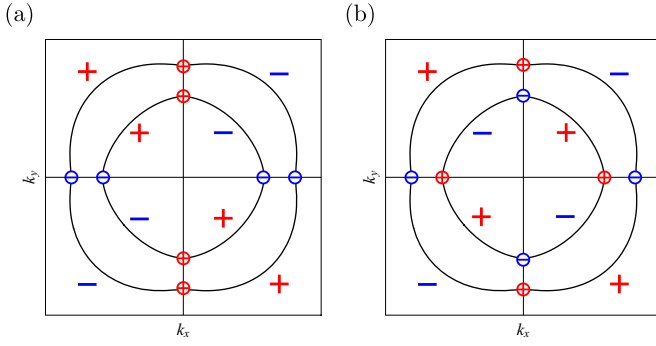\tag{11}
$$

(a)

(b)

FIG. 2. Pairing anisotropy and topological charges in (a) orbitally trivial pairing and (b) orbitally nontrivial pairing in the band basis with only intraband pairing. The solid lines represent the Fermi surface in normal states. The circles represent ± 2 topological charge.

where

$$q(\boldsymbol{k}) = \epsilon_0 \tau_0 \sigma_0 + \gamma_{xy} \tau_z \sigma_0 + \gamma_x \tau_x \sigma_y + \gamma_y \tau_x \sigma_x$$
$$+ i(\Delta_{d,0} \tau_0 + \Delta_{d,z} \tau_z) \sigma_0 \qquad (12)$$

and

$$V = \frac{1}{\sqrt{2}} \begin{bmatrix} \mathbb{I} & -\tau_0 \sigma_y \\ \mathbb{I} & \tau_0 \sigma_y \end{bmatrix}, \qquad (13)$$

where $\mathbb{I} = \tau_0 \sigma_0$ is a 4×4 unit matrix. Note that det $q(\mathbf{k}^*) = 0$ because of the nodal condition $E_-(\mathbf{k}^*) = 0$. In addition, given that chiral symmetry leads to the topological protection discussed here, we mention physically relevant perturbations that preserve and break this symmetry. In particular, the mirror glide plane symmetry-breaking term $M_I = \lambda_I (k_x^2 - k_y^2) \tau_x \sigma_0$ and nematic order $\eta_Q \tau_z \sigma_0$ preserve chiral symmetry, but a Zeeman field $\boldsymbol{h} \tau_0 \cdot \boldsymbol{\sigma}$ does not.

In class DIII, a topological charge can be defined by the winding number [31], which is given by

$$W_{\mathcal{L}} = \frac{1}{2\pi i} \oint_{\mathcal{L}} dk_l \, \text{Tr}[q^{-1}(\boldsymbol{k}) \partial_{k_l} q(\boldsymbol{k})], \qquad (14)$$

where the contour $\mathcal{L}$ is a loop around the nodal point. This charge is an integer $\mathbb{Z}$ invariant. In the problem we are considering, we also have parity symmetry, which ensures a twofold degeneracy of the nodal point. Consequently, the nodes have a $2\mathbb{Z}$ topological charge [32]. We find that the orbitally trivial and orbitally nontrivial gap functions exhibit different nodal charge distributions in momentum space and that a topological transition exists between these two cases.

To understand the different nodal charge distributions between the orbitally trivial and orbitally nontrivial cases (see Fig. 2), it is useful to consider the limit in which the interband pairing can be ignored. This can be achieved in the orbitally trivial case by setting $\Delta_{d,z} = 0$ and in the orbitally nontrivial case by setting $\Delta_{d,0} = 0$ and also requiring that the interband spin-orbit coupling satisfy $|\gamma_i| \ll |\gamma_{xy}|$. When the interband pairing can be ignored, we can consider the nodal points in each band independently. In this case, following Refs. [24,25], Eq. (14) can be simplified to

$$W_{\mathcal{L}^{\pm}} = - \sum_{\boldsymbol{k}_0 \in S_{\mathcal{L}^{\pm}}} \text{sgn}(\partial_{k_l} \xi_{\boldsymbol{k}}^{\pm}|_{\boldsymbol{k}=\boldsymbol{k}_0}) \text{sgn}(\Delta_{\boldsymbol{k}_0}^{\pm}), \qquad (15)$$

where $\xi^{\pm} = \epsilon_0 \pm \sqrt{\gamma_x^2 + \gamma_y^2 + \gamma_{xy}^2}$, $\Delta_{\boldsymbol{k}}^{\pm}$ is the superconducting gap of positive and negative helicity, and the sum is over the set of points $S_{\mathcal{L}^{\pm}}$ given by the intersection of positive- and negative-helicity Fermi surfaces with the one-dimensional contour $\mathcal{L}^{\pm}$. We consider explicitly the topological charges of the adjacent pair of nodal points in the k_x (>0) direction, $(k_x^{*-}, 0)$ and $(k_x^{*+}, 0)$. In the orbitally trivial case, the superconducting gap $\Delta_{\boldsymbol{k}}^{\pm}$ of each band is $\Delta_{\boldsymbol{k}}^{\pm} = -\Delta_{d,0}$. Therefore, two nodal points will have same-sign topological charges, which we call *same-sign pair* states. On the other hand, for the orbitally nontrivial case, $\Delta_{\boldsymbol{k}}^{\pm} \sim \mp \gamma_{xy} \Delta_{d,z}$, so that the two nodal points have opposite-sign topological charges, which we call *opposite-sign pair* states. In general, the pairing state will be a linear combination of the orbitally trivial and orbitally nontrivial gap functions, but it is intuitively clear that the nodes can still be classified as same-sign pair or opposite-sign pair states and a transition between these two topological states can occur. Furthermore, in both cases, as the spin-orbit coupling is decreased, a gapped d_{xy} superconducting state must arise (assuming that $\Delta_{d,z} \neq 0$). The development of this gapped state for opposite-sign pair states is intuitively clear, but this is not the case for same-sign pair states.

To gain a deeper understanding of the physics discussed above, we consider a more general treatment of the topological charge. In particular, the topological charge (14) can be cast in the following form:

$$W_{\mathcal{L}} = \frac{1}{\pi} \oint_{\mathcal{L}} dk_l \, \partial_{\boldsymbol{k}} \tan^{-1}$$
$$\times \left[\frac{2(\epsilon_0 \Delta_{d,0} - \gamma_{xy} \Delta_{d,z})}{\epsilon_0^2 - \gamma_x^2 - \gamma_y^2 - \gamma_{xy}^2 - \Delta_{d,0}^2 + \Delta_{d,z}^2} \right]. \qquad (16)$$

This can be understood as the winding number of the vector $(\epsilon_0^2 - \gamma_x^2 - \gamma_y^2 - \gamma_{xy}^2 - \Delta_{d,0}^2 + \Delta_{d,z}^2, \epsilon_0 \Delta_{d,0} - \gamma_{xy} \Delta_{d,z})$ rotating around the nodal point. The crucial term which determines whether same- or opposite-sign pairs appear is the numerator $\epsilon_0 \Delta_{d,0} - \gamma_{xy} \Delta_{d,z}$ (the denominator $\epsilon_0^2 - \gamma_x^2 - \gamma_y^2 - \gamma_{xy}^2 - \Delta_{d,0}^2 + \Delta_{d,z}^2$ behaves similarly for both same- and opposite-sign pairs). Substituting detailed forms (3), the numerator is given by

$$\epsilon_0 \Delta_{d,0} - \gamma_{xy} \Delta_{d,z} = \begin{cases} -a k_x k_y \Delta_0 & \Delta_2 = 0, \\ \frac{k_x k_y}{k_0^2} \Delta_2 \left[\epsilon_0 - a k_0^2 \frac{\Delta_0}{\Delta_2} \right] & \Delta_2 \neq 0. \end{cases}$$
$$(17)$$

If $\Delta_2 = 0$, the sign of the numerator is the same between the two nodal points $\boldsymbol{k}^{*-}$ and $\boldsymbol{k}^{*+}$, leading to topological charges of opposite signs at the two nodal points, that is, opposite-sign pair states. However, if $\Delta_2 \neq 0$ and the sign of $\epsilon_0 - a k_0^2 \Delta_0 / \Delta_2$ changes between the two nodal point $\boldsymbol{k}^{*-}$ and $\boldsymbol{k}^{*+}$, the topological charges have the same sign at the two nodal points, leading to same-sign pair states. In order to develop an analytic condition to distinguish these two cases, we consider the $k_y = 0$ direction and set $\tilde{k}_x$ as $\epsilon_0(\tilde{k}_x) - a k_0^2 \Delta_0 / \Delta_2 = 0$. In the case of same-sign pair states, $k_x^{*-} < \tilde{k}_x < k_x^{*+}$, this is not satisfied for opposite-sign pair states. With the nodal
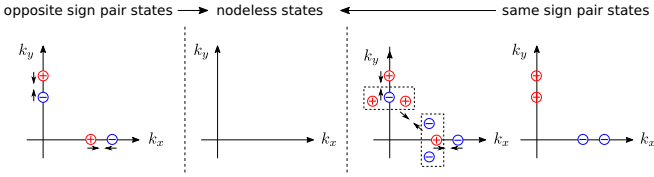
FIG. 3. Schematic picture of transition to nodeless states from *opposite-* (left) and *same -sign pair* states (right). The arrows represent that two nodal points merge with each other. In same-sign pair states, each inner nodal point splits into three nodal points (surrounded by a dashed line) in transition to nodeless states.

condition (7), we get the following inequality:

$$2mv_{\mathrm{so}}^2 - m\sqrt{2\frac{\mu}{m}v_{\mathrm{so}}^2 - \frac{\Delta_0^2}{m^2} + v_{\mathrm{so}}^4} < a\frac{\Delta_0}{\Delta_2}k_0^2$$

$$< 2mv_{\mathrm{so}}^2 + m\sqrt{2\frac{\mu}{m}v_{\mathrm{so}}^2 - \frac{\Delta_0^2}{m^2} + v_{\mathrm{so}}^4}. \qquad (18)$$

As an example, if we take the values $\Delta_0 = 11$ meV and $\Delta_2 = -1.5$ meV, which were used earlier to generate a gap anisotropy consistent with experiment, and assume a strong interband spin-orbit coupling $v_{\mathrm{so}} = 80$ meV Å, then the topological character of nodal points is classified as opposite-sign pair states.

Now we turn to the development of the gapless d_{xy} state due to the merging and annihilation of nodal points. It is worth emphasizing that this has been studied in Dirac and Weyl semimetals [22] and also in *s*- and *d*-wave superconductors [28] in a framework different from ours in which spin-orbit coupling is not an essential interaction. In the case of opposite-sign pair states, the nodal points can merge and are annihilated as the interband spin-orbit coupling decreases because they have opposite topological charges. However, in the case of same-sign pair states, merging and annihilation of nodal points cannot occur directly. We find that this annihilation occurs through an involved mechanism. Indeed, as the interband spin-orbit coupling is decreased from the same-sign pair state (which we take to be positive for both in the description that follows), a new pair of opposite-charge nodal points is created near the nodal point at $\boldsymbol{k}^{*-}$. As the interband spin-orbit coupling is further decreased, the negatively charged nodal point stays near $\boldsymbol{k}^{*-}$, while the two positively charged nodal points move off the k_x (or k_y) axis. The positively charged nodal points that move off the k_x axis eventually merge with similarly formed negatively charged nodal points that have moved off the k_y axis. This leaves an opposite-sign pair state, for which the nodes merge and annihilate as before when the interband spin-orbit coupling is further decreased (see Fig. 3).

B. Andreev flat-band states

We find that, typically, either same-sign pair states or opposite-sign pair states occur when the superconducting state is nodal. In particular, the state we find above with 16 nodal points exists only in a narrow range of parameters, so we do not consider it further here. It would be of interest to be able to experimentally identify whether same-sign or opposite-sign
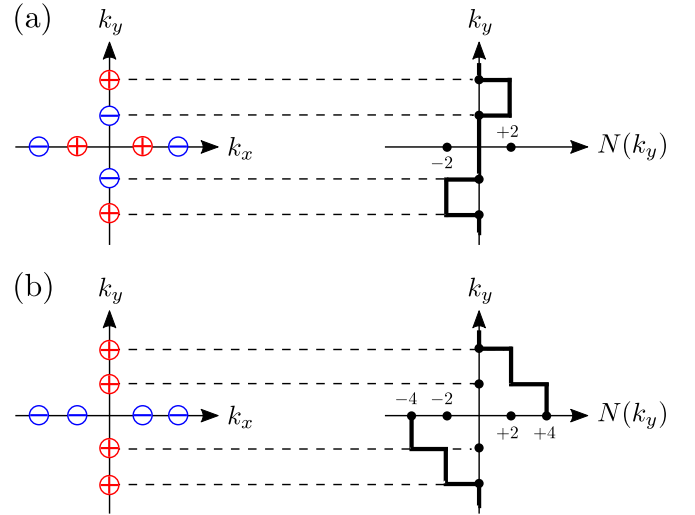

FIG. 4. Schematic pictures of the relation between $W_{\mathcal{L}}$ (left) and $N(k_y)$ (right) in the case of (a) opposite-sign pair and (b) same-sign pair states. Red and blue points indicate $W_{\mathcal{L}} = +2$ and -2, respectively.

pair states exist. As we show below, this can be done through an examination of edge states. Prior to discussing this, we note that the values of the spin-orbit coupling used below are larger than those observed in monolayer FeSe grown on $SrTiO_3$. Consequently, we do not predict flat-band energy states for this material (however, there still exist in-gap edge states that are not topologically protected). In this context we note that the spin-orbit coupling may be larger when monolayer FeSe is grown on a different substrate or if it is doped, for example, with Te, which may allow for the flat-band edge states to be observed.

The nontrivial topological charges at nodal points imply the existence of dispersionless Andreev band states or Andreev flat-band states as edge states. The number of Andreev flat-band states is related to a one-dimensional (1D) winding number $N(\boldsymbol{k}_\parallel)$ [25,33], which is given by

$$N(\boldsymbol{k}_\parallel) = \int d\boldsymbol{k}_\perp \, \mathrm{Tr}[q^{-1}(\boldsymbol{k})\partial_{\boldsymbol{k}_\perp} q(\boldsymbol{k})], \qquad (19)$$

where $\boldsymbol{k}_\parallel$ ($\boldsymbol{k}_\perp$) is the bulk momentum parallel (perpendicular) to the surface. We consider edges running along the y direction and take $\boldsymbol{k}_\parallel$ ($\boldsymbol{k}_\perp$) as k_y (k_x). Figure 4 shows the relation between the 1D winding number $N(k_y)$ and the topological charge $W_{\mathcal{L}}$. Figure 4(a) shows the 1D winding number is nonzero between nodal points which have opposite-sign topological charges but is zero at the origin in the case of opposite-sign pair states. On the other hand, the 1D winding number is nonzero for all momenta between the outer nodal points in the case of same-sign pair states [Fig. 4(b)].

In order to investigate the edge states further, we introduce a lattice model which corresponds to Eq. (2) (see Appendix A). We suppose that the system has two edges at $i_x = 1$ and N_x in the x direction and take the boundary condition in the y direction to be periodic. Then, we examine the edge states by numerically obtaining the energy spectrum as a function of the momentum k_y. We set $N_x =$
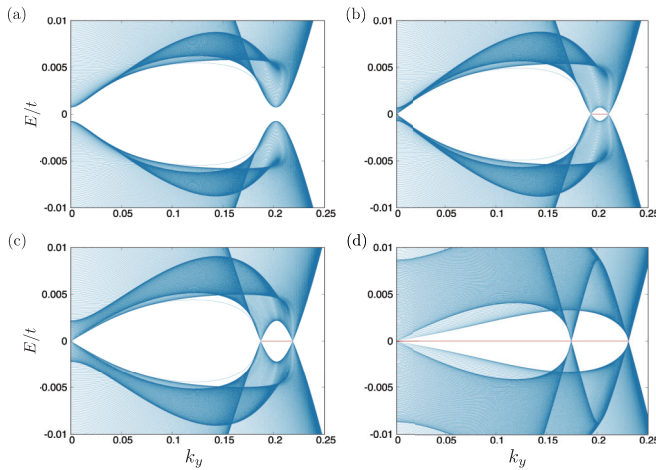
FIG. 5. Energy spectra for (a) no nodal points and (b) opposite-sign pair, (c) opposite-sign pair, and (d) same-sign pair states. We set the parameters (v_{so} [meV Å], Δ_0 [meV], Δ_2 [meV]) as (a) $(50, 11, -1.5)$, (b) $(60, 11, -1.5)$, (c) $(70, 11, -1.5)$, and (d) $(80, 4, -10)$. The vertical axis is scaled by $t = (2m)^{-1}$.
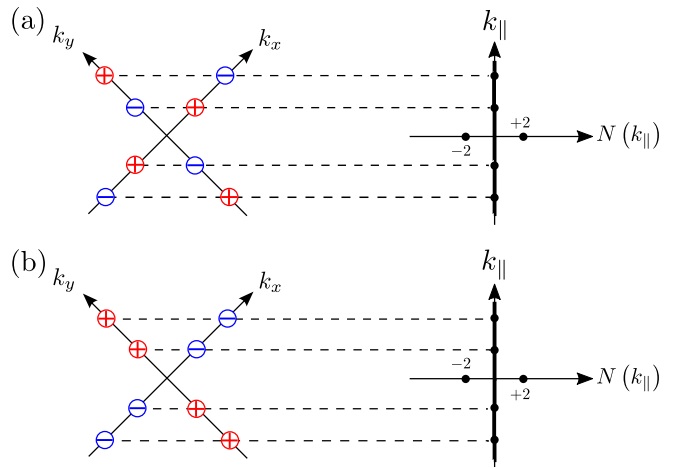

FIG. 6. Schematic pictures of the relation between $W_{\mathcal{L}}$ (left) and $N(k_{\parallel})$ (right) in the case of (a) opposite-sign pair and (b) same-sign pair states. We consider the edges running along the $(1, 1)$ direction. Red and blue points indicate $W_{\mathcal{L}} = +2$ and -2, respectively.

10 000. Figure 5 shows the energy spectra for no nodal points [Fig. 5(a)], opposite-sign pair states [Figs. 5(b) and 5(c)], and same-sign pair states [Fig. 5(d)]. Indeed, with no nodal points we do not have Andreev flat-band states, and once the nodal points appear with increasing interband spin-orbit coupling, flat-band states appear. In the cases of opposite-sign pair states, the flat-band states exist between two nodal points that have opposite topological charges, and the number of the flat-band states is two for each edge. On the other hand, in the cases of same-sign pair states [Fig. 5(d)], the flat-band states exist at $k_y = 0$, and the number of the flat-band states across $k_y = 0$ and between two nodal points in positive k_y is four and two for each edge, respectively. In these cases, the number of flat-band states has a one-to-one correspondence with $|N(k_y)|$, which is shown in Fig. 4. Note that in Fig. 5(d) the finite-size effect creates a gap at $k_y = 0$. We have confirmed that there is no gap at $k_y = 0$ by using the recursive Green's function method (see Appendix B). In addition to the flat-band edge states that appear when nodes exist in the bulk spectrum, note that we find edge states within the gap, although not at zero energy, even in the fully gapped case. These can be attributed to sign changes in the gap that still appear in a fully gapped d_{xy} superconductor.

In actual experiments misalignments would appear, and it is worth mentioning the consequences of this on the distinct topological phases and the resultant anisotropy of the number of Andeev flat bound states. The one-to-one correspondence between the number of flat-band states and $|N(k_{\parallel})|$ is also useful for the edge in other directions. For instance, consider the edges running along the $(1, 1)$ direction and denote the wave-vector component $k_{\parallel}$ parallel to the edges. Figures 6(a) and 6(b) show the 1D winding number $|N(k_{\parallel})|$ and the topological charge $W_{\mathcal{L}}$ for the cases of opposite-sign pair and same-sign pair states, respectively. For both cases $|N(k_{\parallel})| = 0$ for any $k_{\parallel}$; therefore, there are no Andreev flat-band states.

Finally, we note that the examination of the Andreev bound state spectra should take into account interaction effects. It has

been pointed out that due to the large density of states intrinsic to flat bands, they are susceptible to surface instabilities [33,34]. The most likely candidate is edge ferromagnetism that splits the flat bands [34]. Such a surface instability is seen in tunneling spectroscopy experiments on the cuprate superconductor $YBa_2CU_3O_7$ where the zero-bias conductance peak is seen to split into two below an edge transition temperature that is approximately $0.1T_c$ [35]. We leave the study of possible edge instabilities of Andreev flat-band states due to interactions in the context of the models examined here to future work.

IV. CONCLUSION

We have studied nodal topological charges in d-wave superconducting monolayer FeSe to help understand the origin of a fully gapped d-wave state. The nodal points that arise when interband spin-orbit coupling is sufficiently strong have $2\mathbb{Z}$ topological charges that give rise to zero-energy dispersionless Andreev edge bound states. The momentum space distribution of the nodal charges depends strongly on the orbital character of the superconducting state, allowing this to be probed through the observation of Andreev bound states.

APPENDIX A: LATTICE MODEL

In order to obtain the lattice model which corresponds to Eq. (2), we replace $k_i \rightarrow \sin k_i$ and $(k_x^2 + k_y^2)/(2m) \rightarrow -2t(\cos k_x + \cos k_y) + 4t$, where $t^{-1} = 2m$ in Eq. (2)

(the lattice constant is unity). We use $A_{i\sigma}$ and $B_{i\sigma}$, which are annihilation operators of two orbital, spin $\sigma = \uparrow$ and $\downarrow$ electrons at i, and we divide $\mathcal{H}$ into $\mathcal{H}_0$, $\mathcal{H}_{\rm SOC}$, and $\mathcal{H}_\Delta$. They are given by

$$
\begin{aligned}
\mathcal{H}_0 = & -t \sum_{\langle i,j \rangle, \sigma} [A_{i\sigma}^\dagger A_{j\sigma} + B_{i\sigma}^\dagger B_{j\sigma}] - (\mu - 4t) \sum_{i,\sigma} [A_{i\sigma}^\dagger A_{i\sigma} + B_{i\sigma}^\dagger B_{i\sigma}] \\
& + \frac{a}{4} \sum_{i,\sigma} [A_{i\sigma}^\dagger A_{i+x+y\sigma} + A_{i+x+y\sigma}^\dagger A_{i\sigma} - (A_{i\sigma}^\dagger A_{i+x-y\sigma} + A_{i+x-y\sigma}^\dagger A_{i\sigma})] \\
& - \frac{a}{4} \sum_{i,\sigma} [B_{i\sigma}^\dagger B_{i+x+y\sigma} + B_{i+x+y\sigma}^\dagger B_{i\sigma} - (B_{i\sigma}^\dagger B_{i+x-y\sigma} + B_{i+x-y\sigma}^\dagger B_{i\sigma})],
\end{aligned}
\tag{A1}
$$

$$
\begin{aligned}
\mathcal{H}_{\rm SOC} = & -\frac{v_{\rm so}}{2} \sum_i [\{A_{i\uparrow}^\dagger B_{i+x\downarrow} - A_{i+x\uparrow}^\dagger B_{i\downarrow}\} - \{A_{i\downarrow}^\dagger B_{i+x\uparrow} - A_{i+x\downarrow}^\dagger B_{i\uparrow}\} \\
& + \{B_{i\uparrow}^\dagger A_{i+x\downarrow} - B_{i+x\uparrow}^\dagger A_{i\downarrow}\} - \{B_{i\downarrow}^\dagger A_{i+x\uparrow} - B_{i+x\downarrow}^\dagger A_{i\uparrow}\}] \\
& + \frac{v_{\rm so}}{2i} \sum_i [\{A_{i\uparrow}^\dagger B_{i+y\downarrow} - A_{i+y\uparrow}^\dagger B_{i\downarrow}\} + \{A_{i\downarrow}^\dagger B_{i+y\uparrow} - A_{i+y\downarrow}^\dagger B_{i\uparrow}\} \\
& + \{B_{i\uparrow}^\dagger A_{i+y\downarrow} - B_{i+y\uparrow}^\dagger A_{i\downarrow}\} + \{B_{i\downarrow}^\dagger A_{i+y\uparrow} - B_{i+y\downarrow}^\dagger A_{i\uparrow}\}],
\end{aligned}
\tag{A2}
$$

$$
\begin{aligned}
\mathcal{H}_\Delta = & -\frac{\Delta_2}{4k_0^2} \sum_i [A_{i\uparrow}^\dagger A_{i-x-y\downarrow}^\dagger + A_{i\uparrow}^\dagger A_{i+x+y\downarrow}^\dagger - (A_{i\uparrow}^\dagger A_{i-x+y\downarrow}^\dagger + A_{i\uparrow}^\dagger A_{i+x-y\downarrow}^\dagger) \\
& - \{A_{i\downarrow}^\dagger A_{i-x-y\uparrow}^\dagger + A_{i\downarrow}^\dagger A_{i+x+y\uparrow}^\dagger - (A_{i\downarrow}^\dagger A_{i-x+y\uparrow}^\dagger + A_{i\downarrow}^\dagger A_{i+x-y\uparrow}^\dagger)\}] \\
& - \frac{\Delta_2}{4k_0^2} \sum_i [B_{i\uparrow}^\dagger B_{i-x-y\downarrow}^\dagger + B_{i\uparrow}^\dagger B_{i+x+y\downarrow}^\dagger - (B_{i\uparrow}^\dagger B_{i-x+y\downarrow}^\dagger + B_{i\uparrow}^\dagger B_{i+x-y\downarrow}^\dagger) \\
& - \{B_{i\downarrow}^\dagger B_{i-x-y\uparrow}^\dagger + B_{i\downarrow}^\dagger B_{i+x+y\uparrow}^\dagger - (B_{i\downarrow}^\dagger B_{i-x+y\uparrow}^\dagger + B_{i\downarrow}^\dagger B_{i+x-y\uparrow}^\dagger)\}] \\
& + \Delta_0 \sum_i [A_{i\uparrow}^\dagger A_{i\downarrow}^\dagger - A_{i\downarrow}^\dagger A_{i\uparrow}^\dagger - (B_{i\uparrow}^\dagger B_{i\downarrow}^\dagger - B_{i\downarrow}^\dagger B_{i\uparrow}^\dagger)] + \text{H.c.}
\end{aligned}
\tag{A3}
$$

APPENDIX B: ENERGY SPECTRUM USING THE GREEN'S FUNCTION METHOD

Our Hamiltonian matrix of the edge problem has a simple band form,

$$
\mathcal{H} = \begin{pmatrix}
A & B & 0 & 0 & 0 & 0 & \cdot & \cdot \\
B^\dagger & A & B & 0 & 0 & 0 & \cdot & \cdot \\
0 & B^\dagger & A & B & 0 & 0 & \cdot & \cdot \\
0 & 0 & B^\dagger & A & B & 0 & & \\
\cdot & \cdot & \cdot & & & & & \\
\cdot & \cdot & \cdot & & & & &
\end{pmatrix},
\tag{B1}
$$

where A and B are small square matrices of order 8 (or 4 in the reduced block form). Lópes Sancho *et al.* [36] developed a highly convergent iterative scheme to calculate the surface and bulk Green's functions (G_{00} and $G_{\infty\infty}$, respectively) for this form of Hamiltonian. At the ith iteration, the (renormalized) G_{00} is given in terms of effective interaction with the 2^ith layer:

$$
(\omega I - \epsilon_i^s) G_{00} = I + \alpha_i G_{2^i,0},
\tag{B2}
$$

and other elements are given by

$$
(\omega I - \epsilon_i) G_{2^i n,0} = \beta_i G_{2^i (n-1),0} + \alpha_i G_{2^i (n+1),0},
\tag{B3}
$$

$$
(\omega I - \epsilon_i) G_{2^i n, 2^i n} = I + \beta_i G_{2^i (n-1), 2^i n} + \alpha_i G_{2^i (n+1), 2^i n},
\tag{B4}
$$

where ω is an energy with a small imaginary part $i\eta$ and (ω-dependent) energy matrices ϵ_i^s, ϵ_i, α_i, and β_i are determined recursively starting from $\epsilon_0^s = \epsilon_0 = A$, $\alpha_0 = B$, and $\beta_0 = B^\dagger$. As the iteration proceeds, the effective interactions α_i and β_i decay quickly. We take $\eta/t = 10^{-5}$, and the iteration is truncated when $|\alpha_i/t|, |\beta_i/t| < 10^{-7}$. The required number of iterations is at most 20.

Figure 7 shows k_y-resolved spectral functions obtained with this method,

$$
N_n(k_y, E) = -\frac{1}{\pi} \text{Im Tr } G_{nn}(k_y, E + i\eta),
\tag{B5}
$$

with $n = 0$ (edge) and $n = \infty$ (bulk), for the four parameter sets used in Figs. 5(a)–5(d). A blowup of spectral functions near $k_y \sim 0$ is shown in Fig. 8.
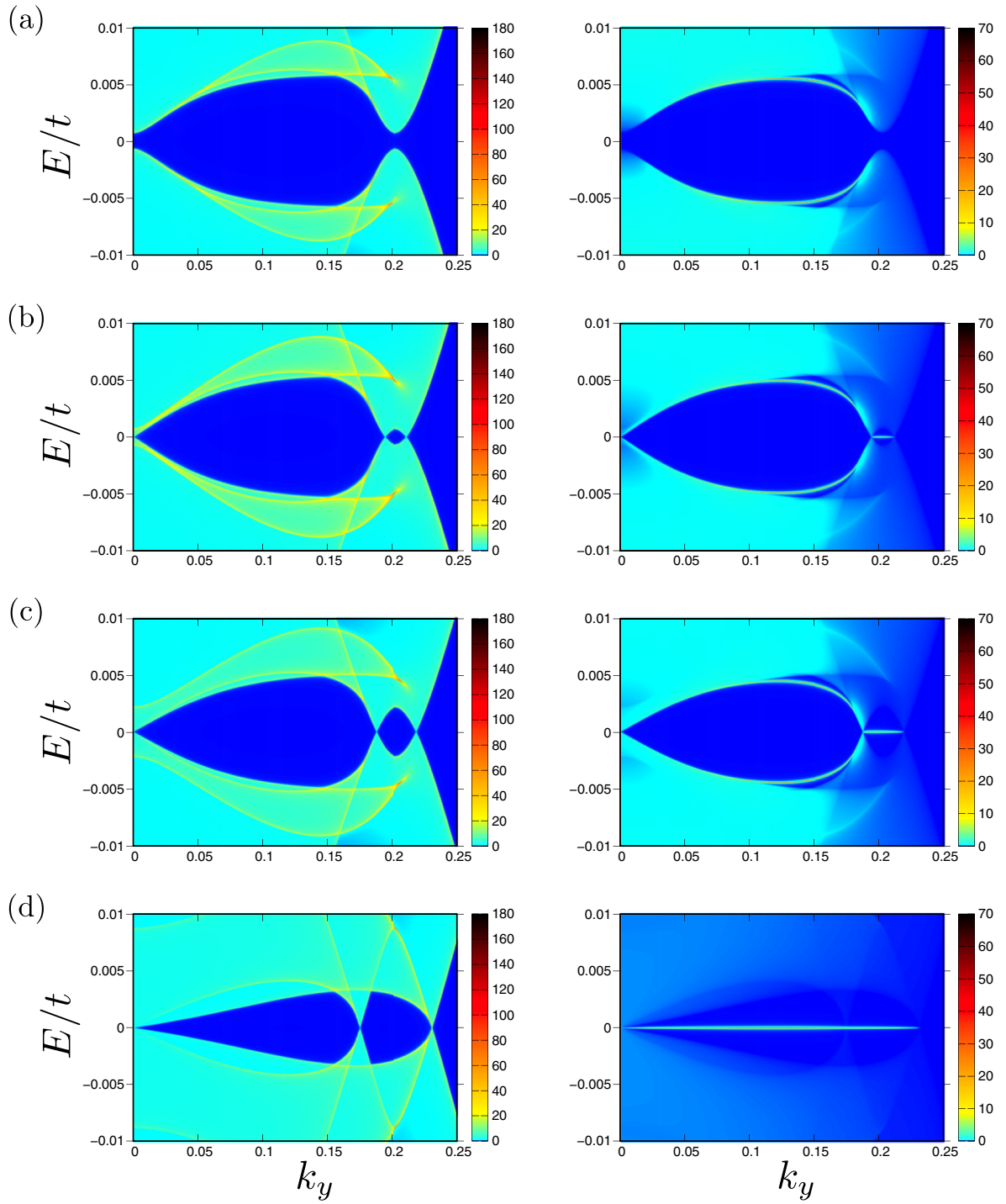
FIG. 7. Momentum-resolved spectral function calculated by the Green's function method. Left (right) panels provide the local density of states at the bulk (edge). The dark blue area represents a no-state region. (a) Full gap, (b) and (c) opposite-sign pairs of nodal points, and (d) same-sign pair of nodal points. The energy is given in units of t.
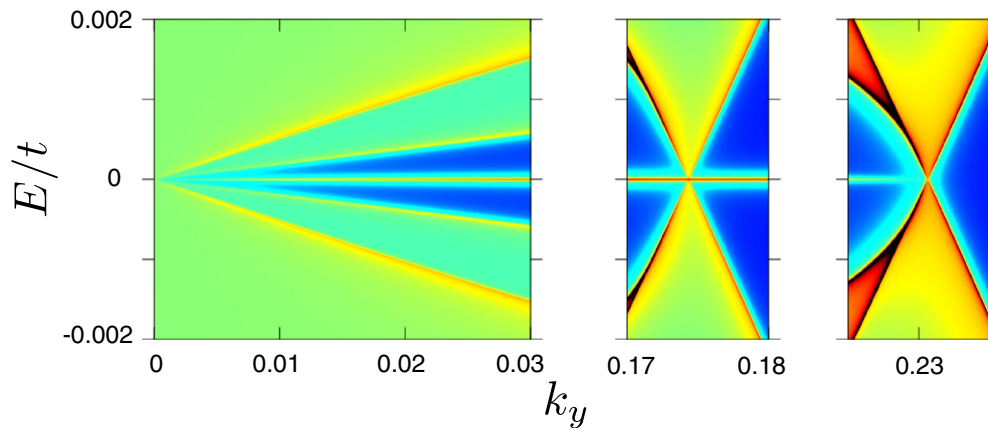
FIG. 8. Blowup of the spectral function (edge+bulk) of the parameter set in Fig. 5(d) around gapless regions with fine resolution in energy and momentum.

[1] Q.-Y. Wang, Z. Li, W.-H. Zhang, Z.-C. Zhang, J.-S. Zhang, W. Li, H. Ding, Y.-B. Ou, P. Deng, K. Chang, J. Wen, C.-L. Song, K. He, J.-F. Jia, S.-H. Ji, Y.-Y. Wang, L.-L. Wang, X. Chen, X.-C. Ma, and Q.-K. Xue, Interface induced high temperature superconductivity in single unit-cell FeSe films on SrTiO$_3$, Chin. Phys. Lett. **29**, 037402 (2012).

[2] Q. Fan, W. H. Zhang, X. Liu, Y. J. Yan, M. Q. Ren, R. Peng, H. C. Xu, B. P. Xie, J. P. Hu, T. Zhang, and D. L. Feng, Plain s-wave superconductivity in single-layer FeSe on SrTiO$_3$ probed by scanning tunneling microscopy, Nat. Phys. **11**, 946 (2015).

[3] Z. Li, J.-P. Peng, H.-M. Zhang, W.-H. Zhang, H. Ding, P. Deng, K. Chang, C.-L. Song, S.-H. Ji, L. Wang, K. He, X. Chen, Q.-K. Xue, and X.-C. Ma, Molecular beam epitaxy growth and post-growth annealing of FeSe films on SrTiO$_3$: A scanning tunneling microscopy study, J. Phys.: Condens. Matter **26**, 265002 (2014).

[4] D. Liu, W. Zhang, D. Mou, J. He, Y.-B. Ou, Q.-Y. Wang, Z. Li, L. Wang, L. Zhao, S. He, Y. Peng, X. Liu, C. Chen, L. Yu, G. Liu, X. Dong, J. Zhang, C. Chen, Z. Xu, J. Hu, X. Chen, X. Ma, Q. Xue, and X. J. Zhou, Electronic origin of high-temperature superconductivity in single-layer FeSe superconductor, Nat. Commun. **3**, 931 (2012).

[5] S. He, J. He, W. Zhang, L. Zhao, D. Liu, X. Liu, D. Mou, Y.-B. Ou, Q.-Y. Wang, Z. Li, L. Wang, Y. Peng, Y. Liu, C. Chen, L. Yu, G. Liu, X. Dong, J. Zhang, C. Chen, Z. Xu, X. Chen, X. Ma, Q. Xue, and X. J. Zhou, Phase diagram and electronic indication of high-temperature superconductivity at 65 K in single-layer FeSe films, Nat. Mater. **12**, 605 (2013).

[6] S. Tan, Y. Zhang, M. Xia, Z. Ye, F. Chen, X. Xie, R. Peng, D. Xu, Q. Fan, H. Xu, J. Jiang, T. Zhang, X. Lai, T. Xiang, J. Hu, B. Xie, and D. Feng, Interface-induced superconductivity and strain-dependent spin density waves in FeSe/SrTiO$_3$ thin films, Nat. Mater. **12**, 634 (2013).

[7] Y. Zhang, J. J. Lee, R. G. Moore, W. Li, M. Yi, M. Hashimoto, D. H. Lu, T. P. Devereaux, D.-H. Lee, and Z.-X. Shen, Superconducting Gap Anisotropy in Monolayer FeSe Thin Film, Phys. Rev. Lett. **117**, 117001 (2016).

[8] I. I. Mazin, D. J. Singh, M. D. Johannes, and M. H. Du, Unconventional Superconductivity with a Sign Reversal in the Order Parameter of LaFeAsO$_{1-x}$F$_x$, Phys. Rev. Lett. **101**, 057003 (2008).

[9] K. Kuroki, S. Onari, R. Arita, H. Usui, Y. Tanaka, H. Kontani, and H. Aoki, Unconventional Pairing Originating from the Disconnected Fermi Surfaces of Superconducting LaFeAsO$_{1-x}$F$_x$, Phys. Rev. Lett. **101**, 087004 (2008).

[10] D. Huang and J. E. Hoffman, Monolayer FeSe on SrTiO$_3$, Annu. Rev. Condens. Matter Phys. **8**, 311 (2017).

[11] S. Coh, M. L. Cohen, and S. G. Louie, Large electron-phonon interactions from FeSe phonons in a monolayer, New J. Phys. **17**, 073027 (2015).

[12] X. Chen, S. Maiti, A. Linscheid, and P. J. Hirschfeld, Electron pairing in the presence of incipient bands in iron-based superconductors, Phys. Rev. B **92**, 224514 (2015).

[13] I. I. Mazin, Symmetry analysis of possible superconducting states in K$_x$Fe$_y$Se$_2$ superconductors, Phys. Rev. B **84**, 024529 (2011).

[14] P. M. Eugenio and O. Vafek, Classification of symmetry derived pairing at the M point in FeSe, Phys. Rev. B **98**, 014503 (2018).

[15] Z.-X. Li, F. Wang, H. Yao, and D.-H. Lee, What makes the T_c of monolayer FeSe on SrTiO$_3$ so high: A sign-free quantum Monte Carlo study, Sci. Bull. **61**, 925 (2016).

[16] D. F. Agterberg, T. Shishidou, J. O'Halloran, P. M. R. Brydon, and M. Weinert, Resilient Nodeless d-Wave Superconductivity in Monolayer FeSe, Phys. Rev. Lett. **119**, 267001 (2017).

[17] T. Shishidou, D. F. Agterberg, and M. Weinert, Magnetic fluctuations in single-layer FeSe, Commun. Phys. **1**, 8 (2018).

[18] Q. Wang, Y. Shen, B. Pan, X. Zhang, K. Ikeuchi, K. Iida, A. D. Christianson, H. C. Walker, D. T. Adroja, M. Abdel-Hafiez, X. Chen, D. A. Chareev, A. N. Vasiliev, and J. Zhao, Magnetic ground state of FeSe, Nat. Commun. **7**, 12182 (2016).

[19] V. Cvetkovic and O. Vafek, Space group symmetry, spin-orbit coupling, and the low-energy effective Hamiltonian for iron-based superconductors, Phys. Rev. B **88**, 134510 (2013).

[20] M. Sigrist and K. Ueda, Phenomenological theory of unconventional superconductivity, Rev. Mod. Phys. **63**, 239 (1991).

[21] M. Z. Hasan and C. L. Kane, Colloquium: Topological insulators, Rev. Mod. Phys. **82**, 3045 (2010).

[22] O. Vafek and A. Vishwanath, Dirac Fermions in Solids: From High-T_c Cuprates and Graphene to Topological Insulators and Weyl Semimetals, Annu. Rev. Condens. Matter Phys. **5**, 83 (2014).

[23] A. P. Schnyder and P. M. R. Brydon, Topological surface states in nodal superconductors, J. Phys.: Condens. Matter **27**, 243201 (2015).

[24] A. P. Schnyder, P. M. R. Brydon, and C. Timm, Types of topological surface states in nodal noncentrosymmetric superconductors, Phys. Rev. B **85**, 024522 (2012).

[25] M. Sato, Y. Tanaka, K. Yada, and T. Yokoyama, Topology of Andreev bound states with flat dispersion, Phys. Rev. B **83**, 224511 (2011).

[26] A. V. Chubukov, O. Vafek, and R. M. Fernandes, Displacement and annihilation of Dirac gap nodes in d-wave iron-based superconductors, Phys. Rev. B **94**, 174518 (2016).

[27] E. M. Nica, R. Yu, and Q. Si, Orbital-selective pairing and superconductivity in iron selenides, npj Quantum Mater. **2**, 24 (2017).

[28] D. V. Chichinadze and A. V. Chubukov, Winding numbers of nodal points in Fe-based superconductors, Phys. Rev. B **97**, 094501 (2018).

[29] G.-Y. Zhu, F.-C. Zhang, and G.-M. Zhang, Proximity-induced superconductivity in monolayer CuO_2 on cuprate substrates, Phys. Rev. B **94**, 174501 (2016).

[30] A. P. Schnyder, S. Ryu, A. Furusaki, and A. W. W. Ludwig, Classification of topological insulators and superconductors in three spatial dimensions, Phys. Rev. B **78**, 195125 (2008).

[31] B. Béri, Topologically stable gapless phases of time-reversal-invariant superconductors, Phys. Rev. B **81**, 134515 (2010).

[32] T. Bzdušek and M. Sigrist, Robust doubly charged nodal lines and nodal surfaces in centrosymmetric systems, Phys. Rev. B **96**, 155105 (2017).

[33] A. P. Schnyder and S. Ryu, Topological phases and surface flat bands in superconductors without inversion symmetry, Phys. Rev. B **84**, 060504(R) (2011).

[34] A. C. Potter and P. A. Lee, Edge Ferromagnetism from Majorana Flat Bands: Application to Split Tunneling-Conductance Peaks in High-T_c Cuprate Superconductors, Phys. Rev. Lett **112**, 117002 (2014).

[35] M. Covington, M. Aprili, E. Paraoanu, L. H. Greene, F. Xu, J. Zhu, and C. A. Mirkin, Observation of Surface-Induced Broken Time-Reversal Symmetry in $YBa_2Cu_3O_7$ Tunnel Junctions, Phys. Rev. Lett. **79**, 277 (1997).

[36] M. P. L. Sancho, J. M. L. Sancho, and J. Rubio, Highly convergent schemes for the calculation of bulk and surface Green functions, J. Phys. F **14**, 1205 (1985).